Non-LTE spectroscopy of the tetradecad region of methane recorded in a hypersonic flow

E. Dudás, B. Vispoel, Robert R. Gamache, Michael M. Rey, V.G. Tyuterev, A. V. Nikitin, S. Kassi, N. Suas-David, R. Georges

Non-LTE spectroscopy of the tetradecad region of methane recorded in a hypersonic flow

Eszter Dudás [a,1], Bastien Vispoel [b], Robert R. Gamache [c], Michaël Rey [d], Vladimir G. Tyuterev [d], Andrei V. Nikitin [e], Samir Kassi [f], Nicolas Suas-David [a], Robert Georges [a,2]

[a] Univ Rennes, CNRS, IPR (Institut de Physique de Rennes) - UMR 6251, F-35000 Rennes, France
[b] Research Unit Lasers and Spectroscopies (LLS), Institute of Life, Earth and Environment (ILEE), University of Namur (UNamur), 61 rue de Bruxelles, B-5000, Namur, Belgium
[c] Department of Environmental, Earth, and Atmospheric Sciences University of Massachusetts Lowell, Lowell, MA 01854 USA
[d] Groupe de Spectrométrie Moléculaire et Atmosphérique, UMR CNRS 7331, BP 1039, Reims Cedex 2, F-51687, France
[e] Laboratory of Theoretical Spectroscopy, V.E. Zuev Institute of Atmospheric Optics, SB RAS, 634055 Tomsk, Russia
[f] Université Grenoble Alpes, LIPhy, F-38000 Grenoble, France and CNRS, LIPhy, F-38000 Grenoble, France

[1)]now at The von Karman Institute for Fluid Dynamics, Waterloosesteenweg 72, B-1640 Sint-Genesisus-Rode, Belgium
[2)]Corresponding author. E-mail address: robert.georges@univ-rennes1.fr

ABSTRACT

Laboratory spectroscopic data is essential for the modeling of hot exoplanet atmospheres, since molecules such as methane, a major component of hot-Jupiter-type exoplanet atmospheres, have a complex vibrational energy structure that makes computational predictions difficult at high temperatures for ro-vibrational transitions involving highly excited vibrational sates. To better inform line lists used in radiative transfer modelling, the ro-vibrational spectrum of methane has been recorded in the tetradecad region between 1.7 and 1.65 µm (5880-6060 cm^{-1}) through non-local thermodynamic equilibrium (non-LTE) cavity ringdown spectroscopy (CRDS). Non-LTE conditions, characterized by a low rotational temperature (~39 K) and a high vibrational temperature (up to 1130 K), have been obtained by hypersonic expansion of a pre-heated mixture of argon and methane in a contoured Laval nozzle. The high vibrational temperature increases the intensity of new hot bands, while the very low rotational temperature greatly simplifies their rotational structure, thus facilitating their identification. A close comparison of the recorded CRDS data to the TheoReTS database reveals both inefficient vibrational relaxation between polyads and efficient vibrational relaxation between vibrational states forming a polyad. These effects result in an overpopulation of the lowest vibrational energy level of each polyad, an effect not widely currently incorporated in non-LTE radiative transfer models. A series of new hot band transitions originating from the pentad and octad polyads were assigned and are provided as a line list for use in future databases.

1. Introduction

Hot Neptune and hot Jupiters (~ 1000 K) are giant planets similar in mass to Neptune or Jupiter orbiting very close to their parent stars [1] and their atmosphere is affected by the presence of methane. These exoplanets are typically tidally locked to the parent star and thus have a face constantly illuminated and a face constantly in darkness. The presence of methane is unlikely on the day side of very hot Jupiters and Neptunes (>2000 K) because the $CO + 3H_2 \leftrightarrow CH_4 + H_2O$ reaction evolves toward the left-hand side at high temperature, but it is expected to be present on the cooler night side [1]. Methane can also be found in the atmosphere of young giant exoplanets (YGE) which are self-luminous jovian planets much further away from their parent stars. Numerous observations across different infrared (IR) bands have now confirmed the presence of methane in the atmosphere of hot Jupiters [2–6], in the atmosphere of YGEs [7,8], but also in the atmosphere of brown dwarfs (see e.g. the study by Oppenheimer *et al.* [9] whose spectra have been used to calibrate hot methane line lists [10,11]).

Two observation methods are currently used. The first method is the transit method, based on the variation of the total flux of the light collected when the planet passes in front of (primary eclipse, transmission spectrum) or behind (secondary eclipse, emission spectrum) its star along our line of sight. The primary eclipse probes the terminator region, i.e. the frontier border between the day and night sides, which revealed the presence of methane in the atmosphere of XO-1b through the observation of transitions in the near-infrared (1.2 – 1.8 µm) icosad and tetradecad regions (see Table 1) [4]. It has also been claimed that methane was detected with this technique in the atmosphere of HD 189733b by observing its band head spectrum at 2.2 µm [3], although this has subsequently been disputed (see for example Gibson *et al.* [12]). Conversely, the secondary eclipse probes the day side of the planet's atmosphere. This latter approach is much more sensitive to thermal gradients, providing access to the temperature profile of the atmosphere. It enabled the first detection of methane on HD 209458b [2] through the tetradecad region and confirmed its presence on HD 189733b [13,14]. Transit method observations were either performed from space with the Hubble Space Telescope using the NICMOS camera [2–4] or from the ground with the SpeX instrument on the NASA Infrared Telescope Facility (IRTF) [13,14]. They cover the mid-IR and near-IR regions, typically between 1.2 and 4.2 µm, but suffer from very low instrumental resolution (R~35 [2–4] or R = 470 [13,14]) making the identification of methane difficult because other molecules, such as water, contribute to the very unstructured measured signals. Observing the spectra of transiting hot Jupiter exoplanets is not, however, limited to low-resolution space-based instruments. High-resolution spectroscopy from ground-based telescopes is also used to detect various molecular species, including CH_4 (see e.g. Giacobbe et al. [15] who confirmed the existence of methane in the atmosphere of HD 209458b). The high accuracy of these observations on the position and intensity of the molecular lines is a guarantee of reliability for the identification of the molecular species surveyed.

The second method of observation is direct imaging of self-luminous planets [16]. This second method is carried out by terrestrial telescopes which observe in the atmospheric transmission windows (K band centered at 2.2 µm or H band centered at 1.65 µm), but also by the recently launched James Webb space telescope (JWST) in the region of the pentad at

3.25 µm, in the 1.66 (tetradecad) and 7-9 µm (dyad) regions (see Table 1) [6]. These telescopes offer high resolutions that make it possible to distinguish the rotational-vibrational structure of the methane spectrum in the atmosphere of YGEs and hot gaseous exoplanets. This was the case for the observation of methane in multiple exoplanets: HR 8799b with the OSIRIS instrument of the Gran Telescopio Canarias (2.2 µm, R ~ 4,000) [7], 51 Eridani b with the Gemini Planet imager Exoplanet Survey GPIES (1.6 – 2.1 µm, R ~ 80) [8], and more recently HD 102195b [5] (while not a transiting planet, HD 120195b has an orbital period of 4.1 days and is therefore not a self-luminous planet) and HD 209458b [15] with the Telescopio Nazionale Galileo (R~ 50,000). The final measurement approaches the maximum resolution typically achievable in laboratory experiments (R ~ 10^6). For comparison, the two infrared spectrometer on JWST have a resolution between 1000 and 3500 [6].

Much information has been extracted from the spectral signatures of methane in the atmosphere of hot Jupiters and YGEs. Observations of methane in the mid-IR highlighted the potential existence [2] or the absence [5] of a temperature inversion on HD 209458b and HR 102195b, respectively. Unexpectedly, the methane spectrum revealed a potential non-LTE emission phenomenon in the 3.3 µm band on HD 189733b [13,14], but this was later disputed by Mandell *et al*. [17]. It is worth mentioning the recent comprehensive study by Wright *et al.* [18] on the calculation of non-LTE spectra of various molecules, including methane, based on ExoMol cross sections and dedicated to exoplanets. Finally, the abundance of methane was used as a probe to deduce the eddy diffusion coefficient of the atmosphere of HR 8799b [7]. However, these observations and deductions require reliable spectral simulations to interpret the data. The first investigations [2–4] are based on absorption coefficients evaluated by combining high temperature data at 800, 1000 and 1273 K from Nassar & Bernath [19] with data from PNNL and the 2004 version of the HITRAN database [20]. However, since the first versions of HITRAN were developed on the basis of experimental data obtained at room temperature (marked by an absence of the numerous hot bands and of high *J* transitions), extrapolation to higher temperatures in fraught with risk. Recognizing this, the authors underline the inadequacy of these databases for probing the modulations of the atmospheric thermal profile and for constraining abundance profiles [4]. Barman *et al.* [7] used the ExoMol database [21], which was presented as the most complete and precise database available in 2014 (It should be noted that the ExoMol methane line list was later replaced by a more comprehensive updated line list up to 2000 K [22]). Meanwhile, a recent study by Guilluy *et al.* [5] used the HITRAN 2012 version. A methane line list suitable for high-temperature calculations up to 3000 K, covering 0-13,400 cm^{-1}, has been recently made available [23,24], as part of the TheoReTS project [25]. Because of the improved reliability and accuracy of the TheoReTS line list, confirmed by recent experimental studies and modeling [26–31], it was used to create the HITEMP spectroscopic database for methane [31].

The present study, part of the e-PYTHEAS [32] and TEMMEX [33] projects, focuses on the region of the 5th polyad of methane (P_4), the tetradecad (see Table 1 and Ref. [34]), consisting of interactions between 14 vibrational states, leading to a set of 60 vibrational sub-levels located between 5400 and 6200 cm^{-1} [35]. It is briefly recalled that the vibrational energy levels of methane are ordered in packets, called polyads (see Table 1), under the effect of the accidental degeneracy linked to the ratios between the frequencies associated with the

molecule's vibrational modes. Thus, for methane, the polyad number P obeys the relation $P=2v_1+v_2+2v_3+v_4$, where v_i are the vibrational quantum numbers associated with normal modes i of the molecule. At high temperature, the infrared spectrum is composed in this region of cold bands but also of numerous hot bands originating from the dyad (P_1), the pentad (P_2) and the octad (P_3), and reaching the icosad (P_5), the triacontad (P_6), and the tetracontad (P_7), respectively. The spectra recently recorded by Ghysels *et al.* [26] in the tetradecad region under LTE conditions at 964 K and by Wong *et al.* [27] at eight temperatures ranging from 295 K up to 1000 K illustrate well the complexity induced by these overlapping contributions.

The cold band transitions $P_4 \leftarrow P_0$ are well known for intermediate *J* values, up to 15 for cold band transitions. Among other studies, they were investigated by FTIR spectroscopy at liquid nitrogen temperature to perform a first global analysis of the tetradecad [35]. A procedure combining liquid nitrogen and room temperature measurements following the so-called 2T-method was also performed to retrieve the lower state energies [36,37]. A detailed analysis of the LTE absorption spectrum of $^{12}CH_4$ in the region 5855–6250 cm^{-1} of the $2v_3$ band has also been reported in Ref. [38]. Additionally, the vibrational states of the icosad involved in the first series of hot band transitions ($P_5 \leftarrow P_1$) were extensively investigated by differential laser absorption spectroscopy [36,39] and cw-cavity ring-down spectroscopy (CRDS) [40,41], and processed using the 2T-method, providing an interesting set of reference data. As a result, it appears that the hot band transitions $P_5 \leftarrow P_1$ are well predicted by variational calculations included in the TheoReTS database [25], in which the line intensities have been computed using *ab initio* dipole moment surfaces [42]. Up to the icosad range the line positions for low and medium *J* values in the TheoReTS line lists were corrected using experimental energy levels as described in Ref. [23].

The difficulty begins with the series of hot transitions $P_6 \leftarrow P_2$ and $P_7 \leftarrow P_3$ which involve the P_6 and P_7 polyads, consisting each of hundreds of interacting vibrational sub-levels (see Table 1), whose modeling remains arduous. The upper part of the triacontad (P_6) and the full tetracontad (P_7) have been investigated by Fourier transform spectroscopy (FTS) at room temperature [43]. High-temperature methane absorption cross-section in LTE conditions were included in the Atlas [27] up to 8900 cm^{-1} (the triacontad range). Both works [27,43] could potentially provide an interesting set of data to model the hot band transition, however corresponding line-by-line assignments are not yet achieved. Partial assignment of FTS spectra at three temperatures from 108 to 298K in the 8850-9180 cm^{-1} region were reported in Ref. [42], but only for limited set of transitions. Last but not least, the sub-Doppler double resonance experiment by Foltynowicz *et al*. [28,44] identifies a useful series of low-*J* transitions belonging to the $P_6 \leftarrow P_2$ set of hot bands.

This article further improves the high temperature experimental data available for methane line lists through the identification of transitions involving the highly excited vibrational states of methane detectable by probing a non-LTE hypersonic flow with CRDS between 1.7 and 1.65 µm (5880-6060 cm^{-1}). The use of hypersonic expansion allows the rotational temperature of methane to be lowered to a few tens of kelvins while limiting the relaxation of its vibrational population to the vibrational ground state, thus allowing the recording of rotationally-cold hot-bands [45]. It should be emphasised that the data produced is intended to be incorporated into high temperature radiative transfer codes for both LTE and non-LTE models.

Table 1.
The first 7 vibrational polyads of methane. The last column gives the number of vibrational levels in the polyad.

Polyad No. (P_x)	Name	Energy range (cm^{-1}/μm)	Vibrational levels	Vibrational sub-levels
P_0	Ground state	0	1	1
P_1	Dyad	1310 – 1533 (7.63 – 6.52)	2	2
P_2	Pentad	2587– 3065 (3.87 – 3.26)	5	9
P_3	Octad	3870 – 4595 (2.57 – 2.18)	8	24
P_4	Tetradecad	5121 – 6124 (1.95 – 1.63)	14	60
P_5	Icosad	6377 – 7650 (1.57 – 1.31)	20	134
P_6	Triacontad	7603 – 9177 (1.32 – 1.09)	30	280
P_7	Tetracontad	8960 – 10430 (1.12 – 0.96)	40	538

2. Experimental setup

The non-LTE methane spectrum was recorded by probing a hypersonic jet of argon and methane with high-resolution CRDS in the 1.7 – 1.65 μm spectral region. Our experimental system is named Spectroscopy of Molecules Accelerated in Uniform Gas flow (SMAUG). Detailed description of the SMAUG experimental setup can be found in previous publications [45,46]. Briefly, the gas mixture consisting of a carrier gas (argon) and the IR active molecule (methane in the present study) were preheated up to 850 ± 100 K in the high enthalpy source (HES) [47] before being expanded through a specially designed contoured Laval nozzle [48] into a low pressures chamber evacuated by a group of roots pumps. By properly adjusting stagnation and discharge pressure, the Laval nozzle produces a remarkably collimated hypersonic flow, which, combined with a low translational temperature, results in both reduced convective and thermal Doppler broadenings. The technique is well-suited to high-resolution spectroscopy compared to a free jet emerging from a circular orifice, which gives atypical broadened absorption line shapes that are difficult to exploit for spectroscopic purposes [49]. The absorption spectrum of the non-LTE methane molecules was recorded with the CRDS laser beam placed perpendicular to the hypersonic flow axis. As highlighted in Fig. 1, such a configuration causes the line of sight of the laser beam to pass through two distinct flow regions, thus both contribute to the recorded absorption spectrum. These flow regions are the isentropic core (IC) containing the non-LTE methane molecules, and the peripheral hot boundary/shear layers (SL) resulting from the combined effect of an incident oblique shock and frictional forces due to the nozzle walls and the deceleration of the high-speed hypersonic flow under the action of the residual static gas in the low-pressure chamber. The shear layer contribution is actually the sum of several hot sliding flow layers characterized by different temperatures and molecular densities, so the conditions describing the shear layer were taken to be the average of all the sub-layers. The Doppler broadening associated with these two regions is very different, providing a convenient way to distinguish the contributions from the isentropic core and the boundary layers (see Fig. 1).

The high-finesse cavity of the CRDS setup (> 200,000, defined as the free spectral range divided by the bandwidth of the resonances) is achieved using two high-reflectivity mirrors (>99.9987%, Layertec) providing a typical ringdown time of τ = 120 µs, equivalent to an absorption pathlength of 450 m when combined with an isentropic core diameter of the hypersonic flow of 10 mm. The spectral ranges 5884–6003 cm^{-1}, 6005-6073 cm^{-1}, 6120–6140 cm^{-1}, and 6193–6219 cm^{-1} were systematically scanned by a series of fibered distributed feedback (DFB) diode lasers. Each of them covers a bandwidth of about 7 nm (~30 cm^{-1}) as they were mounted on a custom made proportional integral differential (PID) temperature stabilizer that controlled the output wavelength by adjusting the diode temperature from −10°C to 60°C. In the reservoir, a flow of 2 slm (liters per minute under standard conditions of pressure and temperature) of CH_4 is mixed with 19 slm of argon at 1040 Torr of stagnation pressure and at around 850 ± 100 K initial temperature, while the expansion chamber is maintained at 0.5 Torr and ambient temperature. Due to difficulties related to the installation of an adequate temperature sensor (the electric current which powers the heat exchanger disturbs the functioning of thermocouples), the stagnation temperature is not known *a priori*, but deduced from the obtained results.

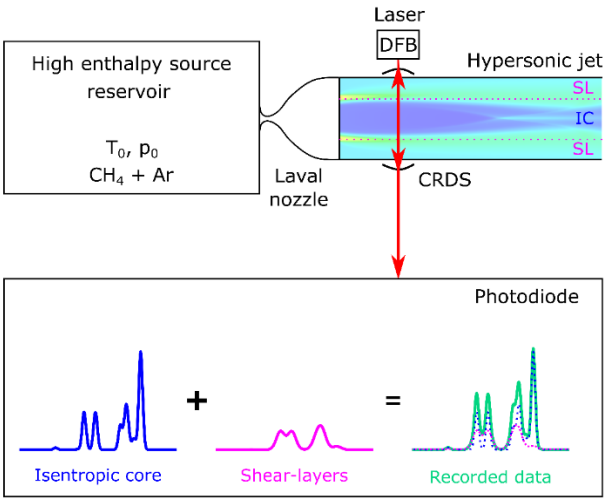

Fig. 1. Schematic representation of the SMAUG experimental setup highlighting the contribution of the isentropic core (IC) and the shear layers (SL) to the recorded spectral data.

3. Simulation of the non-LTE CRDS spectrum from TheoReTS database

In order to identify absorption lines observed for the first time in the tetradecad region of methane, and not yet reported in empirical line lists, the CRDS spectrum (absorption coefficient α in cm^{-1}) was compared to a simulated spectrum generated from the TheoReTS line list [23–25]. For this purpose, the exact experimental conditions were determined, the task complicated by the presence of two contributing flow regions (IC and SL) with unknown molecular densities and different rotational and vibrational temperatures. These physical quantities were extracted by matching the simulation of well-known methane lines to the non-LTE experimental spectrum, according to the procedure described below.

3.1. Non-LTE line intensities

TheoReTS provided transitions of the main isotopologue of methane ($^{12}CH_4$) calculated at 296 K up to the *J* = 20 rotational level, with a cut-off intensity of 10^{-32} cm.molecule^{-1}. In the first step, the reference integrated absorption cross-section (or line intensity) $S_{ij}(T_0)$ at T_0 = 296 K was converted into a corresponding non-LTE absorption cross-section S_{ij}^{nLTE} using:

$$S_{ij}^{nLTE}(T_{rot},T_{vib,\nu_i}) = S_{ij}(T_0)\frac{Q_0(T_0)}{Q_{rot}(T_{rot})\times\tilde{Q}_{vib}(\tilde{T}_{vib})}\times\frac{exp\left[-c_2\left(\frac{E_i^{vib}}{T_{vib,\nu_i}}+\frac{E_i^{rot}}{T_{rot}}\right)\right]}{exp\left(-c_2\frac{E_i}{T_0}\right)}\times\left[\frac{1-exp\left[-c_2\left(\frac{E_j^{vib}-E_i^{vib}}{T_{vib,\nu_i}}+\frac{E_j^{rot}-E_i^{rot}}{T_{rot}}\right)\right]}{1-exp\left(-c_2\frac{\nu_{ij}}{T_0}\right)}\right] \quad (1)$$

Here $Q_0(T_0)$, $Q_{rot}(T_{rot})$ and $\tilde{Q}_{vib}(\tilde{T}_{vib})$ are the LTE, rotational and non-LTE vibrational partition functions, respectively. T_0, T_{rot} and $\tilde{T}_{vib}$ are the standard and characteristic rotational and vibrational temperatures (here the symbol "tilde" is used because the vibrational population does not follow the Boltzmann distribution so that a vibrational temperature cannot be strictly defined in the Boltzmanian sense, see *infra*). E_i denotes the lower energy level of the transition, decomposing into a vibrational and a rotational component, E_i^{vib} and E_i^{rot}, respectively. E_j^{vib} and E_j^{rot} represent the two components of the upper energy level of the transition and c_2 is the second radiation constant given by $c_2 = \frac{h.c}{k}$ = 1.4388 cm K, where h is the Planck constant, k is the Boltzmann constant, and c is the speed of light. The third term of the equation corresponds to the induced emission, where ν_{ij} is the wavenumber of the transition, and it is neglected throughout our simulations since its value is 0.999 for our temperature conditions for a line centered at 6000 cm^{-1}. The following simplified equation was therefore systematically applied:

$$S_{ij}^{nLTE}(T_{rot},T_{vib,\nu_i}) = S_{ij}(T_0)\frac{Q_0(T_0)}{Q_{rot}(T_{rot})\times\tilde{Q}_{vib}(\tilde{T}_{vib})}\times\frac{exp\left[-c_2\left(\frac{E_i^{vib}}{T_{vib,\nu_i}}+\frac{E_i^{rot}}{T_{rot}}\right)\right]}{exp\left(-c_2\frac{E_i}{T_0}\right)} \quad (2)$$

Note that T_{rot} is properly defined since the population of the rotational states were distributed according to the Boltzmann distribution [45]. On the contrary, the vibrational population was not distributed according to the Boltzmann distribution [45], so $T_{vib,i}$ was defined for each lower vibrational level by considering the populations of the vibrational ground state (n_0) and the excited state (n_{ν_i}), according to the following equation:

$$T_{vib,\nu_i} = \frac{hcE_j^{vib}}{kln\left(\frac{g_{\nu_i}n_0}{g_0n_{\nu_i}}\right)} \quad (3)$$

where g_0 and g_{v_i} are the statistical weights of the ground state and the v_i vibrational level, respectively.

3.2. The non-LTE partition function

Systems in a non-LTE state are characterized by the population of the levels deviating from the Boltzmann law while the molecular velocity distribution remains Maxwellian. In this state, the translational, rotational, and vibrational levels of a molecular system adjust to equilibrium at very different rates. For such conditions the populations of the states can no longer be determined by simple Boltzmann statistics but rather by a mixture of collisional reactions and exchange of vibrational quanta. The former can involve both vibrational-thermal and vibrational-vibrational exchanges, and both can involve a multiplicity of levels and exchange partners. Edwards *et al*. [50] has shown that this state can be described with a similar probability formalism as LTE by introducing at each point a set of vibrational temperatures, $T_{vib,\,v_i}$, in place of the kinetic temperature, T (see Eq (3)) in atmospheric modeling. These vibrational temperatures are defined by the vibrational level populations determined by solving the statistical equilibrium equations (SEE), which consider a large number of excited states of different molecular species coupled by a variety of collisional energy exchange processes and by band overlapping, together with a detailed model of atmospheric stratification. The model includes vibrational-thermal (V-T) and vibrational-vibrational (V-V) collisional processes, absorption of solar radiation, exchange of photons between atmospheric layers, and spontaneous emission (for details see Ref. [50] and references therein).

For conditions where the temperatures giving the populations of vibrational and rotational states are different, the determination of the non-LTE partition sum (for full details see Ref. [51]) proceeds by writing the energy of vib-rotational states as $E_{vJ} = E_v + E_J$. The partition sum can be written as

$$Q(T) = \sum_{v,J} g_{vJ} e^{-hc(E_v+E_J)/kT} = \sum_{v} g_v e^{-hc(E_v)/kT} \times \sum_{J} g_J e^{-hc(E_J)/kT} \qquad (4)$$

where $g_{vJ} = g_v\, g_J$ are the vibrational and rotational degeneracies. This is called the product approximation (PA). The total internal partition sum (TIPS) can be written as

$$Q(T_{kin}) = Q_v(T_v) Q_r(T_{kin}) \qquad (5)$$

where T_{kin} is the kinetic temperature and T_v is the set of vibrational temperatures describing the system. The vibrational partition sum is

$$Q_v(T_{kin}) = \sum_{\substack{all \\ vibrational \\ states}} g_v e^{-hcE_v/kT_v} \quad (6)$$

and the rotational partition sum is

$$Q_v(T_{kin}) = \sum_{\substack{all \\ rotational \\ states}} g_J e^{-hcE_J/kT} \quad (7)$$

Because the vibrational levels are in non-LTE the usual expression for the vibrational partition sum, for example, Herzberg's harmonic approximation (HA)[52] and that including anharmonic corrections to the vibrational levels [53], cannot be used. Rewriting Eq. (6) as

$$\tilde{Q}_v(T) = \sum_{\nu_i=1}^{\nu_{max}} g_{\nu_i} e^{-hcE_{\nu_i}/kT_{vib,\nu_i}} \quad (8)$$

where the tilde labels a non-LTE quantity, T is the kinetic temperature and T_{vib,ν_i} is the vibrational temperature for state ν_i. The sum goes up to some maximum vibrational level, v_{max}, that ensures convergence of the sum. The T_{vib,ν_i} are determined for each vibrational state by chemical-dynamical models [50,54–57] or other means (see sections 4.5 and 4.7). It should be noted that many vibrational states are not involved in the chemistry and dynamics that shifts population, so for these states, T_{vib,ν_i} is the kinetic temperature.

For $^{12}CH_4$, an effective Hamiltonian calculation of the ground vibrational state *term values* was done up to J=80, giving values complete to 30,424 cm^{-1} ensuring convergence at all temperatures [51]. The rotational partition sum was computed by direct summation. For $^{13}CH_4$, the rotational constants were from Dang-Nhu *et al.* [58] and were used to compute Q_r values using McDowell's spherical-top formula [59]. For both isotopologues, the vibrational term values were determined to very high levels: 134,152.1 cm^{-1} and 134,152.1 cm^{-1}, respectively. However, given the temperatures of this study a cutoff of 15,000 cm^{-1} will insure convergence of the partition sum.

Rotational partition sums were determined using Eq. (7) or the analytical model from T=1-2500 K [51,60]. These $Q_r(T)_r$ values were used in an in-house-developed FORTRAN code (version: NLTE_TIPS_CH4_2021.for) that rapidly recalls $Q_r(T)_r$. The vibrational term values were put into a file, which includes the T_{vib,ν_i} for each state. This file was called by the code to determine $\tilde{Q}_v(T)$ and the total internal partition sum given by $\tilde{Q}_v(T)Q_r(T)$. The code, which computes the non-LTE TIPS for nine molecules (including methane) of importance in planetary atmospheres, is publically available at zenodo.org [60].

3.3. Simulation of the absorption coefficient

The total absorption coefficient, $\alpha(\nu)$, where ν denotes the wavenumber, was simulated by adding the absorption coefficients relative to the cold (IC) and hot (SL) gas layers of the main isotopologue $^{12}CH_4$ according to Eq. (9). Due to low static pressure in the jet, from 0.05 Torr in the isentropic core region up to 0.5 Torr in the shear layers [45], there was no need to consider pressure broadening. Thus, the CRDS spectrum was simulated by applying a purely Gaussian line shape $g(\nu - \nu_0)$ to the non-LTE calculated line intensities S_{ij}^{nLTE} (see Eq. (2)). The full width at half maximum (FWHM) was set to 0.01 cm^{-1} for the IC and 0.0215 cm^{1} for the SL. The corresponding molecular densities, n_{IC} and n_{SL}, were then adjusted in order to best match the observed spectrum (It should be noted that the value of n_{IC} correctly reflects the density of the isentropic core whose spatial extent along the line of sight is relatively large [45]. In contrast, the situation is more complex for the peripheral gas layers of the flow. The value of n_{SL} is in fact an average value resulting from both a shock layer created at the nozzle outlet and the boundary layer resulting from the friction of the gas on the nozzle walls). Once the correct temperature values and partition functions were established, the exact density values (IC and SL) were easily retrieved by a global adjustment of the calculated line absorption coefficients to the experimental spectrum.

$$\alpha_{sim}^{12}(\nu) = \sum_{^{12}CH_4(IC)} n_{IC}.S_{ij}^{nLTE}.g(\nu - \nu_{ij}) + \sum_{^{12}CH_4(SL)} n_{SL}.S_{ij}^{nLTE}.g(\nu - \nu_{ij}) \quad (9)$$

Both the $^{12}CH_4$ and the $^{13}CH_4$ isotopologues were present in natural abundances in the jet. However, only transitions departing from the ground state were considered for the latter isotopologue, since its natural abundance is 1.07%, meaning the intensity of its hot bands was too weak to contribute significantly to the experimental spectrum. Furthermore, concerning $^{13}CH_4$, an LTE spectrum was simulated at the rotational temperature of the isentropic core and its intensity adjusted to the experimental intensity by using an *ad hoc* constant multiplying factor in Eq. (10). Such a factor was needed since the LTE partition function provided by HITRAN [61] is not adapted to our non-LTE conditions. Thus, the constant contains both the density of $^{13}CH_4$ and the correction for its partition function.

$$\alpha_{sim}(\nu) = \alpha_{sim}^{12}(\nu) + \sum_{^{13}CH_4(IC)} const.S_{ij}^{LTE}.g(\nu - \nu_{ij}) \quad (10)$$

3.4. Non-LTE experimental and simulated spectra

Fig. 2 panel (a), shows the recorded hypersonic jet spectrum (black) and the simulated spectrum (pink) of methane. Altogether, more than 6200 methane absorption lines were

obtained by fitting the experimental data. The missing spectral gaps were due to the lack of available diodes in the laboratory. In addition, the most intense absorption lines are absent from the observed spectrum, while they are clearly visible in the simulated one. This is a consequence of the very high finesse of the optical cavity, which resulted in complete absorption of the light over these strong transitions, saturating the spectrometer. Panel (b) highlights the existence of the two different flow regions (IC and SL) and their very distinct line broadening characteristics, along with the appropriate simulation of each using Eq. (9). The IC lines correspond to low-*J* rotational values ($J_{low} \leq 4$, typically), whereas SL lines are associated with higher-*J* rotational values. As an illustration, the assignments of the strongest lines shown in panel (b) are provided in Table 2. It should be stressed that the absorption lines were simulated using Eq. (10) (which relates to both $^{12}CH_4$ and $^{13}CH_4$ isotopologues) without any adjustment of the line positions provided by the TheoReTS line list. Only the densities of the isotopologues were adjusted to best match the intensity of the simulated spectrum to the intensity of the observed spectrum.

Table 2.

Assignment of the strongest transitions shown in panel (b) of Fig. 2. Column 1: line label according to Fig. 2b; column 2: wavenumber of the transition; columns 3-5: intensities (line integrated absorption cross sections) given at 50, 80 and 400 K under LTE-conditions to illustrate the effect of temperature; column 6: lower energy level; column 7: upper polyad; column 8: vibrational quantum numbers of the upper state; column 9: symmetry of the upper vibrational state; column 10: quantum number (*J*-value) relative to the total rotational angular momentum of the upper state; column 11: ro-vibrational symmetry of the upper state; column 12: lower polyad; column 13: vibrational quantum numbers of the lower state; column 14: symmetry of the lower vibrational state; column 15: *J*-value of the lower state; column 16: ro-vibrational symmetry of the lower state.

IC lines															
Line	ν (cm^{-1})	Intensity ($cm.molec^{-1}$)			E_{low} (cm^{-1})	P_{up}	$(VVVV)_{up}$	$(Cv\ J\ C)_{up}$			P_{low}	$(VVVV)_{low}$	$(Cv\ J\ C)_{low}$		
IC lines		50 K	80 K	400 K		Upper level					Lower level				
IC1	6120.58572	5.660e-23	8.797E-23	3.483E-23	104.77284	4	0210	F2	5	A2	0	0000	A1	4	A1
IC2	6121.13002	3.840e-23	5.969E-23	2.364E-23	104.77470	4	0210	F2	5	F2	0	0000	A1	4	F1
IC3	6121.35334	2.844e-23	4.420E-23	1.750E-23	104.77603	4	0210	F2	5	E	0	0000	A1	4	E
IC4	6121.68309	5.457e-23	8.483E-23	3.359E-23	104.78001	4	0210	F2	5	F1	0	0000	A1	4	F2
SL lines															
SL1	6123.00241	< e-28	1.197e-22	1.371E-22	689.70539	4	0020	F2	12	F2	0	0000	A1	11	F1
SL2	6123.58901	1.424e-28	1.913e-22	2.192E-22	689.86232	4	0020	F2	12	A1	0	0000	A1	11	A2
SL3	6124.05689	1.241e-28	1.670e-22	1.915E-22	689.95685	4	0020	F2	12	F2	0	0000	A1	11	F1
SL4	6124.16057	< e-28	1.187e-22	1.360E-22	689.86232	4	0020	F2	12	A1	0	0000	A1	11	A2

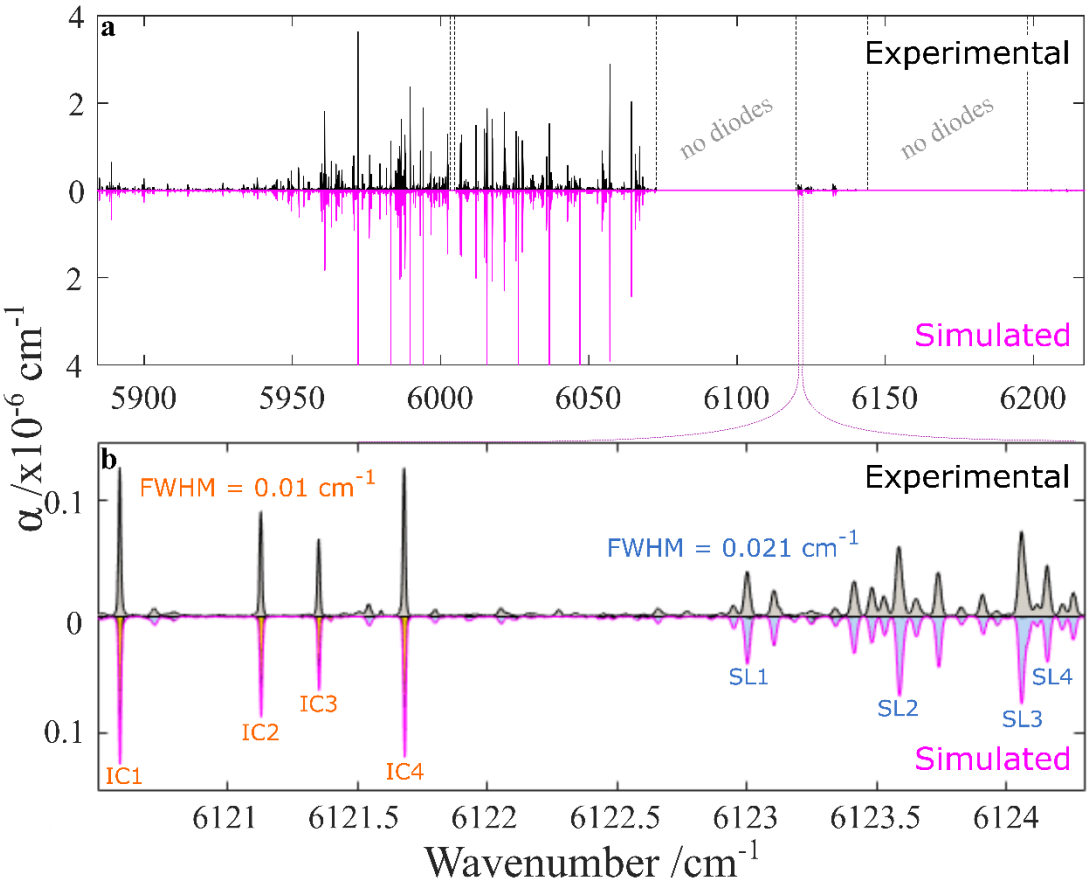

Fig. 2. Observed and simulated spectra of methane. Panel a: Experimental (black) *vs* simulated (pink) non-LTE hypersonic jet spectrum of methane, note that the strongest absorption lines are not observed (see text). Panel b shows part of the spectrum demonstrating the influence of the two different flow regions. The orange lines correspond to the isentropic core (IC) meanwhile the blue lines indicate the contribution of the shear layer (SL). The IC transitions start from low *J*-values (J_{low}=4) while the SL transitions start from higher *J*-values (J_{low}=11).

3.5. Temperature extraction

The rotational and vibrational temperatures of the different flow regions must be specified with care to correctly simulate the experimental spectrum. The notion of vibrational temperature is ambiguous here since the vibrational population, contrarily to the rotational one [55], does not follow Boltzmann's distribution law. In practice, see Eq. (3), the population ratio between the excited vibrational level and the ground state leads to a vibrational temperature which is specific to each particular vibrational level, so that it is necessary to define as many vibrational temperatures as there are significantly populated vibrational energy levels.

Secondarily, the rotational and non-LTE vibrational partition functions have to be determined. This is an iterative process, in which the rotational temperature (T_{rot}) is initially established and the corresponding rotational partition function $Q_{rot}(T_{rot})$ is calculated using the non-LTE TIPS code (NLTE_TIPS_2021) [51,62]. This is followed by the determination of the vibrational temperatures ($T_{vib,v_i}^{IC/SL}$) that serve as the input data for the partition function code

that differentiates all the vibrational levels and their different symmetries and calculates a non-LTE vibrational partition function $\tilde{Q}_{vib}(\tilde{T}_{vib})$.

3.6. Rotational temperatures

As it is mentioned above, one rotational temperature was sufficient to describe either of the flow-regions (IC and SL), indicating an efficient rotational relaxation of the methane molecules in the jet. In our study, the rotational temperature was derived from the relative intensities of the absorption lines belonging to a same vibrational band. This approach has the advantage of avoiding the explicit computation of the rotational partition function at this stage of the analysis. From a practical point of view, the ratio between two integrated absorption coefficients is equal to the ratio between two integrated absorption cross sections and so Eq. (1) leads to Eq. (11), in the particular case of two R(0) and R(1) rovibrational transitions:

$$\frac{\alpha_{R0}}{\alpha_{R1}} = \frac{S_{R0}(T_{rot})}{S_{R1}(T_{rot})} = \frac{S_{R0}(T_0)}{S_{R1}(T_0)} exp\left(c_2 \frac{E_{J=1}^{rot} - E_{J=0}^{rot}}{T_{rot}}\right) \Big/ exp\left(c_2 \frac{E_{J=1}^{rot} - E_{J=0}^{rot}}{T_0}\right) \qquad (11)$$

From transitions departing from J = 0, 1 and 2, the rotational temperature of the isentropic core was determined to be T_{rot}^{IC} = 39 ± 5 K, while transitions $J \geq 7$ are used to obtain the rotational temperature of the shear-layers: T_{rot}^{SL} = 375 ± 25 K, as illustrated in Fig. 3. Since the experimental setup has an instrumental upper limit which saturates the lines that are too intense, in particular the low-J lines of the cold bands, unsaturated low-J lines from the $^{13}CH_4$ isotopologue were chosen to retrieve the rotational temperature of the isentropic core. As can be seen in Figure 3a, the R(0), R(1), R(2) and R(3) lines of the $^{13}CH_4$ isotopologue are narrow because they originate predominantly from the cold gas of the isentropic core of the flow, and in contrast to the lines of the main isotopologue $^{12}CH_4$, they are well isolated, with no overlap with other transitions (cold and hot bands of the main isotopologue of the isentropic core and/or of the shear layers) and are therefore ideal for a reliable extraction of the rotational temperature of the isentropic core. The higher J-value transitions of the $^{13}CH_4$ isotopologue are too weak to be measured accurately, so the ro-vibrational transitions P(7), P(8), P(9) and P(10) of the main isotopologue $^{12}CH_4$ were used to extract the rotational temperature of the shear layers, as shown in Fig. 3b.

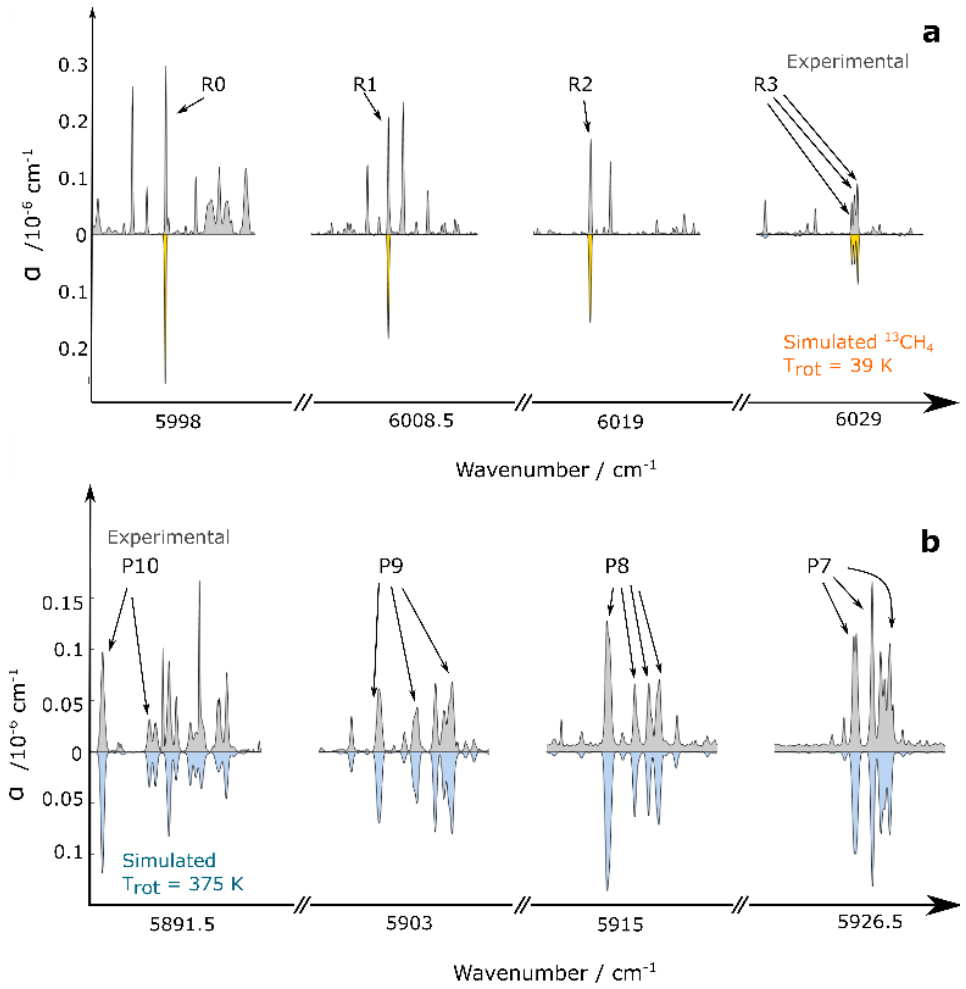

Fig. 3. Determination of the rotational temperatures using tetradecad – GS transitions. Panel (a): simulated $^{13}CH_4$ lines of low-*J* rotational levels to obtain the rotational temperature of the isentropic core. Panel (b): simulated $^{12}CH_4$ lines of higher-*J* rotational levels to determine the rotational temperature of the shear-layer.

3.7. Vibrational temperatures – dyad

The same strategy is applied to calculate the vibrational temperatures, but this time the absorption coefficient of rovibrational transitions starting from an excited vibrational level (hot band transitions α_{ν_i}) are compared to rovibrational transitions issuing from the ground state (GS) (cold band transitions α_{GS}). Eq. (12), resulting from Eq. (2), is applied to a sufficient number of rovibrational transitions to retrieve a reliable vibrational temperature (T_{vib,ν_i}) for each vibrational state ν_i (either ν_4 or ν_2 in the case of the dyad):

$$\frac{\alpha_{GS}}{\alpha_{\nu_i}} = \frac{S_{GS}(T_0)}{S_{\nu_i}(T_0)} \times \frac{\exp\left[c_2.E_i^{rot,GS}\left(\frac{1}{T_0}-\frac{1}{T_{rot}}\right)\right]}{\exp\left[\frac{c_2.E_i^{rot,vi}}{T_0}-c_2.\left(\frac{E_{\nu_i}^{vib}}{T_{vib,\nu_i}}+\frac{E_i^{rot,\nu_i}}{T_{rot}}\right)\right]}, \quad (12)$$

where $E_i^{rot,GS}$ is the energy of the lower rotational energy level of the cold band, E_i^{rot,ν_i} is the rotational energy of the lower rotational energy level of the hot band starting from the ν_i

vibrational state, and $E_{v_i}^{vib}$ denotes the vibrational energy of the lower vibrational energy level of the hot band.

This method works well for the vibrational states of the dyad (P_1 polyad of methane) for which the TheoReTS *ab initio* line list is sufficiently accurate for direct identification and comparison between calculated and experimental fitted lines. In this way, the dyad polyad in the isentropic core can be described with two vibrational temperatures T_{vib,v_4}^{IC} = 877(100) K and T_{vib,v_2}^{IC} = 334(21) K, reflecting a much stronger intra-polyad vibrational relaxation than inter-polyad relaxation. The population of the ν_2 state located at 1533 cm^{-1} partially empties on the first ν_4 state of the polyad located at 1310 cm^{-1} which does not, or only slightly, relaxes down to the GS. These results agree well with the observation of previous studies conducted on slit jet expansion flows with high stagnation temperatures [63,64]. Fig. 4 compares the different vibrational population probabilities under LTE conditions in a reservoir heated to 800 K (red) and under the actual non-LTE conditions in the hypersonic jet (blue). Under LTE 800 K conditions, the population is distributed over more than 30 rotational levels, resulting in a lower percentage of population probabilities for each individual rotational level and therefore relatively weak absorption line intensities. Thus, the strong rotational relaxation in the hypersonic jet not only simplifies the rotational structure of the spectrum, but at the same time provides much more intense absorption lines. Concerning the inter-polyad relaxation, there seems to be no significant relaxation of the population of the dyad down to the GS, which is in good agreement with the former observations by Bronnikov *et al.* [63]. This is summarized in panel (c) of Fig. 4, where the intensities of P(5) transitions starting from the ground state are comparable to P(3) and P(4) transitions issuing from the ν_4 vibrational state. At the same time, the non-relaxation from one polyad to another along with an efficient intra-polyad relaxation leads to effective vibrational temperatures which can be much higher than the stagnation temperature, which contributes to an increase in intensity of the transitions originating from the first state of each polyad.

The shear layers can be described with similar vibrational temperatures T_{vib,v_4}^{SL} = 797(175) K and T_{vib,v_2}^{SL} = 730(166) K. This suggests that the different frictional – and probably turbulent – processes in the shear-layers result in a higher frequency of molecular collisions compared to the isentropic core, favoring vibrational-rotation and vibrational-translation energy transfer between molecules.

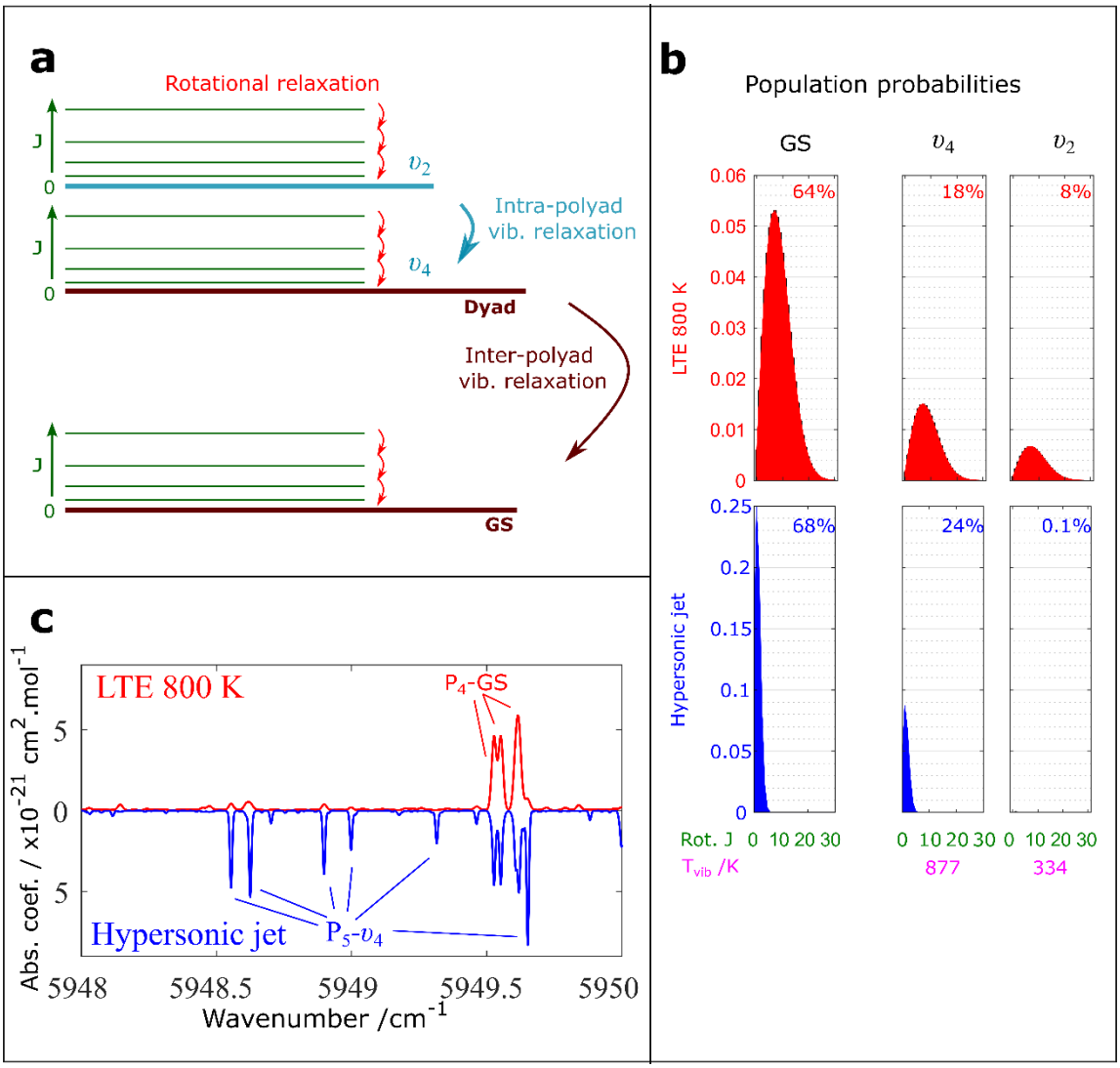

Fig. 4. Representation of the occurring vibrational relaxations. (a): Schematic illustration of the ro-vibrational energy structure of the dyad polyad of methane, highlighting the occurring relaxation types. (b): simulated comparison of the rotational and vibrational population probabilities between LTE 800 K (red) and hypersonic jet (blue) conditions. (c): simulated spectra under LTE 800 K (red) and hypersonic jet (blue) conditions emphasizing the magnified P_5-ν_4 transitions in the hypersonic jet expansion (where P_5 denotes the icosad).

3.8. Vibrational temperatures – pentad

At first, recently experimentally identified hot band transitions [44] starting from the ν_3 vibrational state were targeted with the non-LTE CRDS experiment. However, none of them were observed, although they correspond to low-*J* rotational transitions. As depicted in panel (a) of Fig. 5, the pentad polyad consists of 9 close sub-vibrational levels which facilitates efficient intra-polyad relaxation, therefore explaining the absence of these particular transitions. Considering the signal-to-noise ratio of the experiment, the absence of transitions starting from this vibrational state sets a maximum vibrational temperature T_{vib,ν_3}^{IC} of 500 K, above this temperature the transitions would have been detectable in the recorded spectrum.

The next spectral targets were a small number of transitions belonging to the 0030 ← 0000 cold band ($3\nu_3$ ← GS) involving the triacontad (P_6 polyad), reported in Ref. [42] and in the HITRAN database [65]. The knowledge of the precise position of the final vibrational energy level, in this case the $3\nu_3$, allowed the prediction of precisely calculated line positions starting from the pentad and ending on this particular upper energy level. These specific transitions were used to associate a vibrational temperature to the first two vibrational states of the pentad: $T^{IC}_{vib,2\nu_4(A1)}$ = 1130 ± 91 K and $T^{IC}_{vib,2\nu_4(F2)}$ = 860 ± 100 K.

Unfortunately, due to the lack of other reliable rovibrational transitions, it was not possible to experimentally determine the vibrational temperature associated with the other vibrational states of the pentad. It was therefore decided to consider a "local" Boltzmann distribution population within the vibrational energy levels forming the pentad. The population of the different energy levels, and their associated temperature, was thus extrapolated by considering the same intra-polyad relaxation as occurred between the $2\nu_4(A1)$ and $2\nu_4(F2)$ states. These assumed temperatures, presented in Fig. 5 (in grey), were used as input values for the calculation of the non-LTE vibrational partition function. As a remark, this extrapolation leads to $T^{IC}_{\nu_3}$ = 212 K which is consistent with the limit of 500 K set for the ν_3 vibrational level. Fig. 5 further highlights the strong "intra-polyad" relaxation responsible for an accumulation of the polyad population onto the $2\nu_4(A1)$ lowest vibrational state of the polyad, which is more than 4 times higher for the non-LTE hypersonic jet than it would be under LTE conditions. It is remarkable that the vibrational temperature associated with $2\nu_4(A1)$ is much higher than the initial temperature of the gas before its expansion.

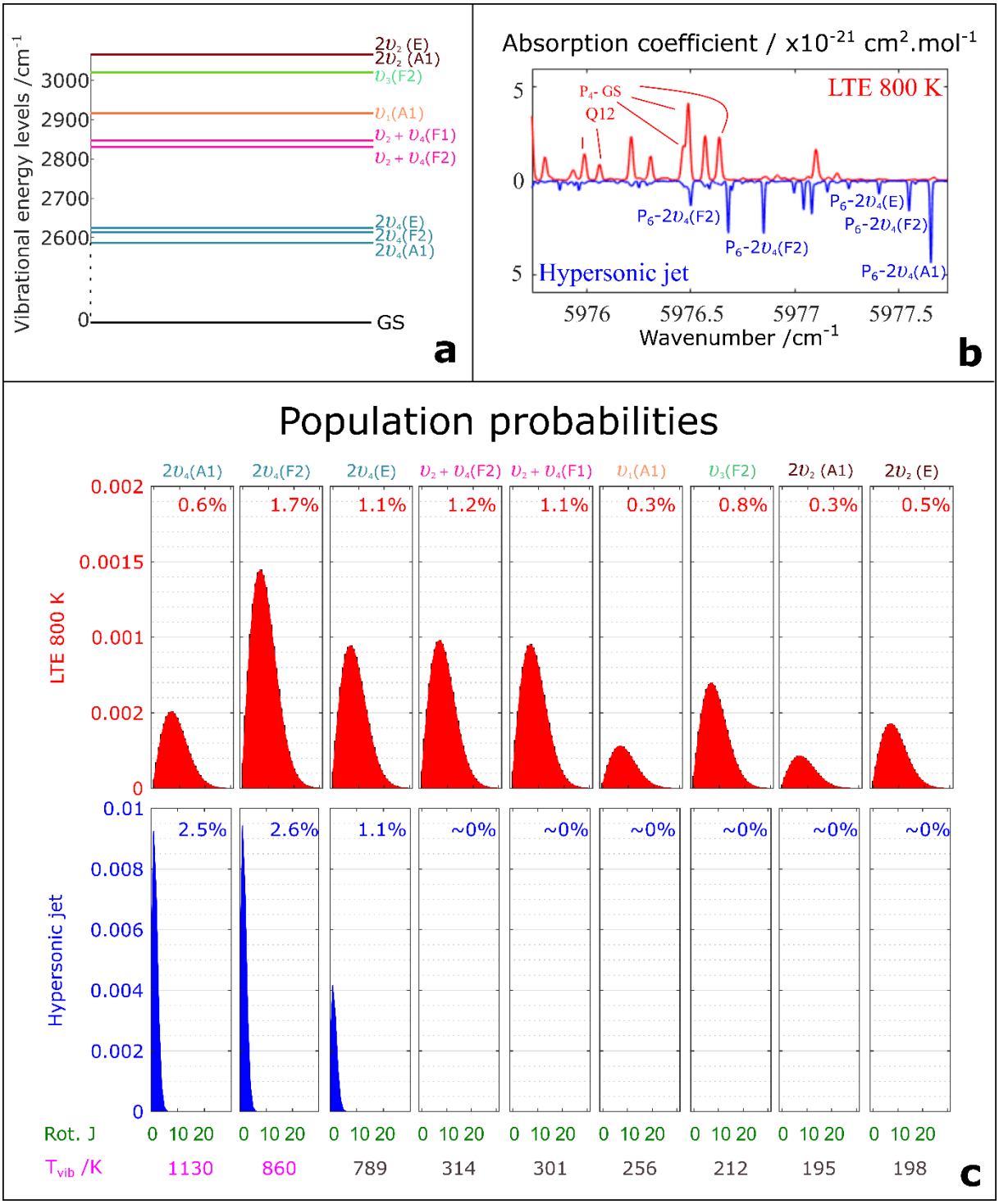

Fig. 5. Representation of the occurring vibrational relaxations. Panel (a): Schematic illustration of the ro-vibrational energy structure of the pentad polyad of methane. Panel (b): simulated spectra under LTE 800 K (red) and hypersonic jet (blue) conditions emphasizing the magnified $P_6 - 2\nu_4$ transitions in the hypersonic jet expansion (where P_6 denotes the triacontad), the symmetry species F2, E, A1 concern the lower vibrational levels. Panel (c): simulated comparison of the rotational and vibrational population probabilities between LTE 800 K (red) and hypersonic jet (blue) conditions.

4. Experimental spectrum *versus ab initio* predictions among highly excited polyads $P_6 \leftarrow P_2$ and $P_7 \leftarrow P_3$

Once the different temperatures were determined, the experimental spectrum was carefully compared to a simulation carried out using the data available in the TheoReTS database. Our objective was to test the robustness of the *ab initio* model used in TheroReTS at high temperature, with particular attention paid to hot band transitions. A previous experimental investigation [44] confirmed that the calculated line positions of transitions starting from the pentad and the octad and ending in energy levels up to 9000 cm^{-1} have an uncertainty of ± 1 cm^{-1} at the most, while the calculated *ab initio* line intensities are accurate to within a few percent [24]. This meant that once the vibrational temperatures were correctly determined, the simulated pattern of the spectrum would match the experimental spectrum in intensity, if not in wavenumber. In this way, pairs of experimental and simulated absorption lines with matching intensities could be identified within the given wavenumber uncertainty interval of ±1 cm^{-1} (see Fig. 6). Pending a more systematic investigation, this protocol was applied to a series of few spectral regions. A set of 22 new hot band transitions is listed in Table 3 and tentatively assigned. The pairing process is illustrated in Fig. 6 where the pink line corresponds to the simulated non-LTE spectrum. The red, blue and green sticks mark the transitions starting from the $2v_4(A1)$, $2v_4(F2)$, and $3v_4(F2)$ states, respectively. Due to the effective intra-polyad relaxation and ineffective inter-polyad relaxation, even transitions starting from the lowest energy vibrational state of the octad were detectable and could be correctly simulated with a vibrational temperature of $T^{IC}_{3v_4(F2)}$ = 1195(80) K.

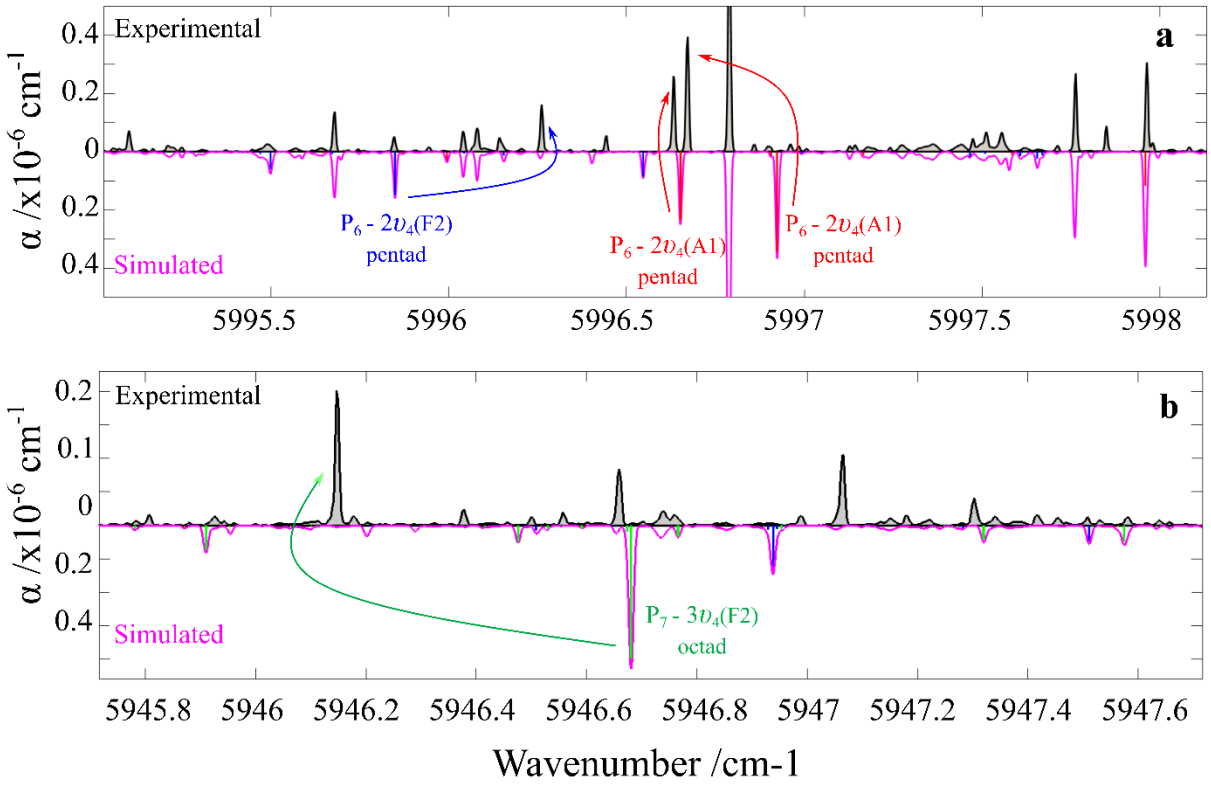

Fig. 6. Illustration of the hot band line assignment protocol based on uncertainty windows of ±1 cm^{-1} around presumptive line candidates. Panel (a): hot band lines stating from the pentad polyad and connecting to the triacontad (P_6), either from the $2v_4(A1)$ (marked by a red stick in the simulation) or the $2v_4(F2)$ (marked by a blue stick in the simulation) vibrational level. Panel (b): hot band line stating from the octad polyad from the $3v_4(F2)$ vibrational level and connecting to the tetracontad (P_7). The lower vibrational levels have F2 or A1 symmetry.

Based on the determined temperature values, the corresponding rotational and non-LTE vibrational functions could be delivered by the NLTE_TIPS_CH4_2021 code provided by Gamache *et al.*[51,60]. Knowledge of the partition functions of methane in the isentropic core and shear-layers made it possible to retrieve the molecular density in each of these flow regions. Thus, it appears that the main contribution to the recorded spectra came from the isentropic core with a molecular density of n_{ic} = 4.95x10^{13} molec.cm^{-3}, confirming the good sensitivity of the SMAUG apparatus as well as showing its power in the characterization of hypersonic flows. The shear-layers had a lower average density of n_{sl} = 0.89x10^{13} molec.cm^{-3}, which lead to the non-negligible hot gas contribution to the absorption spectrum.

Table 3. Newly assigned hot band transitions starting from the pentad and the octad polyads. ν(obs), ν(calc) are the observed and calculated (TheoReTS) wavenumbers of the ro-vibrational transitions, respectively; ν(obs-calc) is the difference between observed and calculated line positions; S: Line intensity retrieved from the simulated spectrum according to Eq. (9). Subscripts "low" and "up" refer to the lower and upper energy levels, respectively. E: ro-vibrational energy level; J: quantum number for total rotational angular momentum; C: ro-vibrational symmetry (product of the rotational and vibrational symmetries); n: ranking number for a given (J,C,P) block; P: Polyad number defined as $P=2v_1+v_2+2v_3+v_4$; A: Einstein coefficient of the transition; vib: vibrational quantum numbers and vibrational symmetry.

ν (obs)	ν (calc)	ν (obs-calc)	S (calc)	E_{low}	J_{up}	C_{up}	n_{up}	P_{up}	J_{low}	C_{low}	n_{low}	P_{low}	E_{up}	A	vib_{up}					vib_{low}				
cm^{-1}	cm^{-1}	cm^{-1}	$cm.molec^{-1}$	cm^{-1}									cm^{-1}	s^{-1}										
5944.5371	5944.4737	0.0635	7.42E-28	2618	1	F1	133	6	2	F2	1	2	8562	0.436	0	0	2	2	F2	0	0	0	2	A1
5944.6768	5944.8985	-0.2216	3.81E-28	2618	1	E	85	6	2	E	1	2	8563	0.335	0	0	2	2	F2	0	0	0	2	A1
5961.3179	5961.4245	-0.1066	1.36E-27	2620	1	A2	49	6	2	A1	1	2	8581	0.486	0	0	2	2	F2	0	0	0	2	F2
5965.0586	5964.6783	0.3803	2.48E-27	2649	3	A1	92	6	3	A2	1	2	8613	0.437	0	0	2	2	F2	0	0	0	2	A1
5965.2863	5965.2041	0.0822	8.42E-28	2618	2	E	142	6	2	E	1	2	8583	0.448	0	0	2	2	F2	0	0	0	2	A1
5965.3234	5965.3579	-0.0346	1.31E-27	2618	2	F1	206	6	2	F2	1	2	8583	0.464	0	0	2	2	F2	0	0	0	2	A1
5965.7126	5965.6481	0.0645	7.09E-28	2597	1	F2	123	6	1	F1	1	2	8563	0.379	0	0	2	2	F2	0	0	0	2	A1
5970.3077	5970.4199	-0.1122	2.28E-27	2620	2	A2	67	6	2	A1	1	2	8590	0.492	0	0	2	2	E	0	0	0	2	F2
5985.8290	5985.8834	-0.0544	1.10E-27	2597	2	F2	217	6	1	F1	1	2	8583	0.355	0	0	2	2	F2	0	0	0	2	A1
5996.6331	5996.6521	-0.0190	9.51E-28	2618	3	E	197	6	2	E	1	2	8615	0.365	0	0	2	2	F2	0	0	0	2	A1
5996.6715	5996.9236	-0.2521	1.40E-27	2618	3	F1	302	6	2	F2	1	2	8615	0.358	0	0	2	2	F2	0	0	0	2	A1
6008.5537	6008.9804	-0.4267	2.56E-27	2649	4	A1	134	6	3	A2	1	2	8658	0.357	0	0	2	2	F2	0	0	0	2	A1
6021.1464	6021.1545	-0.0080	2.74E-28	2587	1	A2	52	6	0	A1	1	2	8608	0.085	0	2	1	2	F2	0	0	0	2	A1
6194.2019	6194.2016	0.0003	3.00E-30	2597	1	F2	182	6	1	F1	1	2	8792	0.0015	0	1	2	1	F2	0	0	0	2	A1
6195.2306	6195.2281	0.0025	6.00E-30	2587	1	A2	69	6	0	A1	1	2	8782	0.0021	1	3	0	1	F2	0	0	0	2	A1
6205.5748	6205.5738	0.0010	8.00E-30	2587	1	A2	70	6	0	A1	1	2	8793	0.0026	0	1	2	1	F2	0	0	0	2	A1
6211.6026	6211.6052	-0.0026	9.00E-30	2597	2	F2	321	6	1	F1	1	2	8809	0.0031	0	1	2	1	F2	0	0	0	2	A1
6215.8802	6215.8794	0.0008	4.70E-30	2649	3	F1	460	6	2	F2	3	2	8865	0.0015	0	1	2	1	E	0	0	0	2	F2
5909.9222	5910.5396	-0.6174	2.61E-30	3928	2	A2	93	7	3	A1	1	3	9839	0.319	0	0	2	3	E	0	0	0	3	F2
5937.8722	5938.3309	-0.4587	3.23E-32	4048	4	F1	648	7	4	F2	10	3	9987	0.0066	0	0	2	3	F2	0	0	0	3	F1
5946.1482	5946.6810	-0.5328	2.28E-30	3872	1	A1	55	7	1	A2	1	3	9818	0.356	0	0	2	3	F1	0	0	0	3	F2
5960.4952	5961.7383	-1.2431	3.39E-30	3872	2	A1	105	7	1	A2	1	3	9833	0.320	0	0	2	3	F2	0	0	0	3	F2

5. Conclusion and perspectives

Through the analysis of the recorded CH_4 non-LTE spectrum, the rotational, intra-polyad and inter-polyad relaxations have been characterized quantitatively. The rotation is well relaxed according to a Boltzmann distribution with a temperature of 39 K. The extracted vibrational temperatures reflect an efficient intra-polyad relaxation that depopulates the high vibrational levels within the polyads, whereas the relaxation between polyads is considerably weaker, which leads to an accumulation of the vibrational population on the first state of each polyad (namely $\nu_4(A1)$, $2\nu_4(A1)$, $3\nu_4(F2)$, etc.). At the same time, it is clearly demonstrated that the population of the symmetrically degenerated vibrational levels (e.g. $2\nu_4(A1)$ and $2\nu_4(F2)$ for the pentad) should be described with different vibrational temperatures in non-LTE conditions. They must therefore be distinguished as if they were completely independent vibrational levels.

The SMAUG setup can produce vibrationally hot and rotationally cold high-resolution infrared spectra of methane. The obtained vibrational temperatures, some above the reservoir temperature, underline the vital features of the experimental setup. Namely, that significant rotational and intra-polyad relaxation ensure the detection of lines corresponding to transitions issuing from pentad and octad by boosting the population in the base vibrations of these polyads. At the same time, these relaxations eliminate a tremendous number of spectral lines from the investigated spectrum and permit the precise analysis of those remaining. A planar Laval nozzle is currently being designed for SMAUG to increase the absorption path length through the cold isentropic core and maximize the cold gas contribution. Future work will consist of systematically assigning the remaining lines recorded in the non-LTE spectrum which most likely belong to hot band transitions starting from vibrational energy levels of the dyad, pentad and octad polyads. This will allow the further refinement of the TheoReTS line list for the simulation of methane spectra at high temperatures relevant to hot Jupiters, in both LTE and non-LTE conditions. As recently pointed out by Wright *et al.* [18], non-LTE conditions can occur in the upper atmosphere of hot Jupiters. The case of HD 189733b, an exoplanet that contains methane, is particularly interesting. The very large temperature differential between its day and night sides appears to cause very fast jet streams at high altitudes [66]. Extremely fast vertical winds have also been modelled in the atmosphere of this exoplanet [67,68]. It is tempting to make a link with our hypersonic laboratory experiment as the temperature drop following the acceleration of these atmospheric layers could be accompanied by a non-LTE state due to the partial relaxation of the vibrational degrees of freedom of methane.

Acknowledgments

The support from ANR e-PYTHEAS project funded by the French Research National Agency (grant ANR-16-CE31-0005), and from ANR-RNF TEMMEX project (grants ANR-21-30CE-0053-01 and RSF 22-42-09022 for the Tomsk research team) is acknowledged. The GSMA laboratory of Reims University, France, acknowledges a support from SAMIA collaborative program. B. Vispoel acknowledges le Fond de la Recherche Scientifique (F.R.S._FNRS) for the post-doctoral

financial support. The authors thank Dr. Thomas S. Hearne for his careful reading of the manuscript.

References

[1] Tinetti G, Encrenaz T, Coustenis A. Spectroscopy of planetary atmospheres in our Galaxy. Astron Astrophys Rev 2013;21:63. https://doi.org/10.1007/s00159-013-0063-6.

[2] Swain MR, Tinetti G, Vasisht G, Deroo P, Griffith C, Bouwman J, et al. Water, methane, and carbon dioxide present in the dayside spectrum of the exoplanet HD 209458b. Astrophys J 2009;704:1616–21. https://doi.org/10.1088/0004-637X/704/2/1616.

[3] Swain MR, Vasisht G, Tinetti G. The presence of methane in the atmosphere of an extrasolar planet. Nature 2008;452:329–31. https://doi.org/10.1038/nature06823.

[4] Tinetti G, Deroo P, Swain MR, Griffith CA, Vasisht G, Brown LR, et al. PROBING THE TERMINATOR REGION ATMOSPHERE OF THE HOT-JUPITER XO-1b WITH TRANSMISSION SPECTROSCOPY. Astrophys J 2010;712:L139–42. https://doi.org/10.1088/2041-8205/712/2/L139.

[5] Guilluy G, Sozzetti A, Brogi M, Bonomo AS, Giacobbe P, Claudi R, et al. Exoplanet atmospheres with GIANO - II. Detection of molecular absorption in the dayside spectrum of HD 102195b. Astron Astrophys 2019;625:A107. https://doi.org/10.1051/0004-6361/201834615.

[6] Miles BE, Biller BA, Patapis P, Worthen K, Rickman E, Hoch KKW, et al. The JWST Early Release Science Program for Direct Observations of Exoplanetary Systems II: A 1 to 20 Micron Spectrum of the Planetary-Mass Companion VHS 1256-1257 b 2022. https://doi.org/10.48550/arXiv.2209.00620.

[7] Barman TS, Konopacky QM, Macintosh B, Marois C. SIMULTANEOUS DETECTION OF WATER, METHANE, AND CARBON MONOXIDE IN THE ATMOSPHERE OF EXOPLANET HR 8799 b. Astrophys J 2015;804:61. https://doi.org/10.1088/0004-637X/804/1/61.

[8] Macintosh B, Graham JR, Barman T, De Rosa RJ, Konopacky Q, Marley MS, et al. Discovery and spectroscopy of the young jovian planet 51 Eri b with the Gemini Planet Imager. Science 2015;350:64–7. https://doi.org/10.1126/science.aac5891.

[9] Oppenheimer BR, Kulkarni SR, Matthews K, Nakajima T. Infrared Spectrum of the Cool Brown Dwarf Gl 229B. Science 1995;270:1478–9. https://doi.org/10.1126/science.270.5241.1478.

[10] Yurchenko SN, Tennyson J, Bailey J, Hollis MDJ, Tinetti G. Spectrum of hot methane in astronomical objects using a comprehensive computed line list. Proc Natl Acad Sci 2014;111:9379–83. https://doi.org/10.1073/pnas.1324219111.

[11] Tannock ME, Metchev S, Hood CE, Mace GN, Fortney JJ, Morley CV, et al. A 1.46–2.48 μm spectroscopic atlas of a T6 dwarf (1060 K) atmosphere with IGRINS: first detections of H2S and H2, and verification of H2O, CH4, and NH3 line lists. Mon Not R Astron Soc 2022;514:3160–78. https://doi.org/10.1093/mnras/stac1412.

[12] Gibson NP, Pont F, Aigrain S. A new look at NICMOS transmission spectroscopy of HD 189733, GJ-436 and XO-1: no conclusive evidence for molecular features. Mon Not R Astron Soc 2011;411:2199–213. https://doi.org/10.1111/j.1365-2966.2010.17837.x.

[13] Swain MR, Deroo P, Griffith CA, Tinetti G, Thatte A, Vasisht G, et al. A ground-based near-infrared emission spectrum of the exoplanet HD 189733b. Nature 2010;463:637–9. https://doi.org/10.1038/nature08775.

[14] Waldmann IP, Tinetti G, Drossart P, Swain MR, Deroo P, Griffith CA. GROUND-BASED NEAR-INFRARED EMISSION SPECTROSCOPY OF HD 189733B. Astrophys J 2011;744:35. https://doi.org/10.1088/0004-637X/744/1/35.

[15] Giacobbe P, Brogi M, Gandhi S, Cubillos PE, Bonomo AS, Sozzetti A, et al. Five carbon- and nitrogen-bearing species in a hot giant planet's atmosphere. Nature 2021;592:205–8. https://doi.org/10.1038/s41586-021-03381-x.

[16] Janson M, Bergfors C, Goto M, Brandner W, Lafrenière D. SPATIALLY RESOLVED SPECTROSCOPY OF THE EXOPLANET HR 8799 c. Astrophys J 2010;710:L35–8. https://doi.org/10.1088/2041-8205/710/1/L35.

[17] Mandell AM, Deming LD, Blake GA, Knutson HA, Mumma MJ, Villanueva GL, et al. NON-DETECTION OF L-BAND LINE EMISSION FROM THE EXOPLANET HD189733b. Astrophys J 2011;728:18. https://doi.org/10.1088/0004-637X/728/1/18.

[18] Wright SOM, Waldmann I, Yurchenko SN. Non-local thermal equilibrium spectra of atmospheric molecules for exoplanets. Mon Not R Astron Soc 2022;512:2911–24. https://doi.org/10.1093/mnras/stac654.

[19] Nassar R, Bernath P. Hot methane spectra for astrophysical applications. J Quant Spectrosc Radiat Transf 2003;82:279–92. https://doi.org/10.1016/S0022-4073(03)00158-4.

[20] Rothman LS, Jacquemart D, Barbe A, Chris Benner D, Birk M, Brown LR, et al. The HITRAN 2004 molecular spectroscopic database. J Quant Spectrosc Radiat Transf 2005;96:139–204. https://doi.org/10.1016/j.jqsrt.2004.10.008.

[21] Yurchenko SN, Tennyson J. ExoMol line lists – IV. The rotation–vibration spectrum of methane up to 1500 K. Mon Not R Astron Soc 2014;440:1649–61. https://doi.org/10.1093/mnras/stu326.

[22] Yurchenko SN, Amundsen DS, Tennyson J, Waldmann IP. A hybrid line list for CH4 and hot methane continuum. Astron Astrophys 2017;605:A95. https://doi.org/10.1051/0004-6361/201731026.

[23] Rey M, Nikitin AV, Bézard B, Rannou P, Coustenis A, Tyuterev VG. New accurate theoretical line lists of 12CH4 and 13CH4 in the 0–13400 cm−1 range: Application to the

modeling of methane absorption in Titan's atmosphere. Icarus 2018;303:114–30. https://doi.org/10.1016/j.icarus.2017.12.045.

[24] Rey M, Nikitin AV, Tyuterev VG. Accurate Theoretical Methane Line Lists in the Infrared up to 3000 K and Quasi-continuum Absorption/Emission Modeling for Astrophysical Applications. Astrophys J 2017;847:105. https://doi.org/10.3847/1538-4357/aa8909.

[25] Rey M, Nikitin AV, Babikov YL, Tyuterev VG. TheoReTS – An information system for theoretical spectra based on variational predictions from molecular potential energy and dipole moment surfaces. J Mol Spectrosc 2016;327:138–58. https://doi.org/10.1016/j.jms.2016.04.006.

[26] Ghysels M, Vasilchenko S, Mondelain D, Béguier S, Kassi S, Campargue A. Laser absorption spectroscopy of methane at 1000 K near 1.7 μm: A validation test of the spectroscopic databases. J Quant Spectrosc Radiat Transf 2018;215:59–70. https://doi.org/10.1016/j.jqsrt.2018.04.032.

[27] Wong A, Bernath PF, Rey M, Nikitin AV, Tyuterev VG. Atlas of Experimental and Theoretical High-temperature Methane Cross Sections from $\less$i$\greater$T$\less$/i$\greater$ = 295 to 1000 K in the Near-infrared. Astrophys J Suppl Ser 2019;240:4. https://doi.org/10.3847/1538-4365/aaed39.

[28] Foltynowicz A, Rutkowski L, Silander I, Johansson AC, Silva de Oliveira V, Axner O, et al. Sub-Doppler Double-Resonance Spectroscopy of Methane Using a Frequency Comb Probe. Phys Rev Lett 2021;126:063001. https://doi.org/10.1103/PhysRevLett.126.063001.

[29] Bézard B, Charnay B, Blain D. Methane as a dominant absorber in the habitable-zone sub-Neptune K2-18 b. Nat Astron 2022;6:537–40. https://doi.org/10.1038/s41550-022-01678-z.

[30] Rannou P, Coutelier M, Rivière E, Lebonnois S, Rey M, Maltagliati L. Convection behind the Humidification of Titan's Stratosphere. Astrophys J 2021;922:239. https://doi.org/10.3847/1538-4357/ac2904.

[31] Hargreaves RJ, Gordon IE, Rey M, Nikitin AV, Tyuterev VG, Kochanov RV, et al. An Accurate, Extensive, and Practical Line List of Methane for the HITEMP Database. Astrophys J Suppl Ser 2020;247:55. https://doi.org/10.3847/1538-4365/ab7a1a.

[32] Etude des hydrocarbures en émission et absorption dasn les exoplanètes à haute température. Agence Natl Rech n.d. https://anr.fr/Projet-ANR-16-CE31-0005 (accessed October 6, 2022).

[33] Méthodes de spectroscopie moléculaire théoriques et expérimentales pour des conditions extrêmes : étude approfondie des signatures spectrales de petits hydrocarbures et radicaux. Agence Natl Rech n.d. https://anr.fr/Projet-ANR-21-CE30-0053 (accessed October 6, 2022).

[34] Albert S, Bauerecker S, Boudon V, Brown LR, Champion J-P, Loëte M, et al. Global analysis of the high resolution infrared spectrum of methane 12CH4 in the region from 0 to 4800cm−1. Chem Phys 2009;356:131–46. https://doi.org/10.1016/j.chemphys.2008.10.019.

[35] V. Nikitin A, Boudon V, Wenger C, Albert S, R. Brown L, Bauerecker S, et al. High resolution spectroscopy and the first global analysis of the Tetradecad region of methane 12 CH 4. Phys Chem Chem Phys 2013;15:10071–93. https://doi.org/10.1039/C3CP50799H.

[36] Kassi S, Gao B, Romanini D, Campargue A. The near-infrared (1.30–1.70 µm) absorption spectrum of methane down to 77 K. Phys Chem Chem Phys 2008;10:4410–9. https://doi.org/10.1039/B805947K.

[37] Gao B, Kassi S, Campargue A. Empirical low energy values for methane transitions in the 5852–6181cm−1 region by absorption spectroscopy at 81K. J Mol Spectrosc 2009;253:55–63. https://doi.org/10.1016/j.jms.2008.09.005.

[38] Nikitin AV, Chizhmakova IS, Rey M, Tashkun SA, Kassi S, Mondelain D, et al. Analysis of the absorption spectrum of 12CH4 in the region 5855–6250 cm−1 of the 2ν3 band. J Quant Spectrosc Radiat Transf 2017;203:341–8. https://doi.org/10.1016/j.jqsrt.2017.05.014.

[39] Sciamma-O'Brien E, Kassi S, Gao B, Campargue A. Experimental low energy values of CH4 transitions near 1.33µm by absorption spectroscopy at 81K. J Quant Spectrosc Radiat Transf 2009;110:951–63. https://doi.org/10.1016/j.jqsrt.2009.02.004.

[40] Wang L, Kassi S, Liu AW, Hu SM, Campargue A. The 1.58µm transparency window of methane (6165–6750cm−1): Empirical line list and temperature dependence between 80 and 296K. J Quant Spectrosc Radiat Transf 2011;112:937–51. https://doi.org/10.1016/j.jqsrt.2010.11.015.

[41] Mondelain D, Kassi S, Wang L, Campargue A. The 1.28 µm transparency window of methane (7541–7919 cm−1): empirical line lists and temperature dependence (80 K–300 K). Phys Chem Chem Phys 2011;13:7985–96. https://doi.org/10.1039/C0CP02948C.

[42] Nikitin AV, Protasevich AE, Rey M, Serdyukov VI, Sinitsa LN, Lugovskoy A, et al. Improved line list of 12CH4 in the 8850–9180 cm−1 region. J Quant Spectrosc Radiat Transf 2019;239:106646. https://doi.org/10.1016/j.jqsrt.2019.106646.

[43] Béguier S, Liu AW, Campargue A. An empirical line list for methane near 1µm (9028–10,435cm−1). J Quant Spectrosc Radiat Transf 2015;166:6–12. https://doi.org/10.1016/j.jqsrt.2015.07.003.

[44] Foltynowicz A, Rutkowski L, Silander I, Johansson AC, Silva de Oliveira V, Axner O, et al. Measurement and assignment of double-resonance transitions to the 8900--9100-${\mathrm{cm}}^{\ensuremath{-}1}$ levels of methane. Phys Rev A 2021;103:022810. https://doi.org/10.1103/PhysRevA.103.022810.

[45] Dudás E, Suas-David N, Brahmachary S, Kulkarni V, Benidar A, Kassi S, et al. High-temperature hypersonic Laval nozzle for non-LTE cavity ringdown spectroscopy. J Chem Phys 2020;152:134201. https://doi.org/10.1063/5.0003886.

[46] Louviot M, Suas-David N, Boudon V, Georges R, Rey M, Kassi S. Strong thermal nonequilibrium in hypersonic CO and CH4 probed by CRDS. J Chem Phys 2015;142:214305. https://doi.org/10.1063/1.4921893.

[47] Georges R, Thiévin J, Benidar A, Carles S, Amyay B, Louviot M, et al. High enthalpy source dedicated to quantitative infrared emission spectroscopy of gas flows at elevated temperatures. Rev Sci Instrum 2019;90:093103. https://doi.org/10.1063/1.5097696.

[48] Georges R, Dudás E, Suas-David N, Rutkowski L. Infrared Absorption Spectroscopy in Laval Nozzle Supersonic Flows. Unif. Supersonic Flows Chem. Phys., WORLD SCIENTIFIC (EUROPE); 2021, p. 479–538. https://doi.org/10.1142/9781800610996_0009.

[49] Suas-David N, Kulkarni V, Benidar A, Kassi S, Georges R. Line shape in a free-jet hypersonic expansion investigated by cavity ring-down spectroscopy and computational fluid dynamics. Chem Phys Lett 2016;659:209–15. https://doi.org/10.1016/j.cplett.2016.06.082.

[50] Edwards DP, López-Puertas M, Gamache RR. The non-LTE correction to the vibrational component of the internal partition sum for atmospheric calculations. J Quant Spectrosc Radiat Transf 1998;59:423–36. https://doi.org/10.1016/S0022-4073(97)00125-8.

[51] Gamache RR, Vispoel B, Rey M, Tyuterev V, Barbe A, Nikitin A, et al. Partition sums for non-local thermodynamic equilibrium conditions for nine molecules of importance in planetary atmospheres. Icarus 2022;378:114947. https://doi.org/10.1016/j.icarus.2022.114947.

[52] Herzberg G. Molecular spectra and molecular structure. II, Infrared and Raman spectra of polyatomic molecules. Toronto: D. Van Nostrand Company; 1945.

[53] Gamache RR, Roller C, Lopes E, Gordon IE, Rothman LS, Polyansky OL, et al. Total internal partition sums for 166 isotopologues of 51 molecules important in planetary atmospheres: Application to HITRAN2016 and beyond. J Quant Spectrosc Radiat Transf 2017;203:70–87. https://doi.org/10.1016/j.jqsrt.2017.03.045.

[54] Edwards DP, López-Puertas M, López-Valverde MA. Non-local thermodynamic equilibrium studies of the 15-μm bands of CO2 for atmospheric remote sensing. J Geophys Res Atmospheres 1993;98:14955–77. https://doi.org/10.1029/93JD01297.

[55] López-Puertas M, López-Valverde MA, Taylor FW. Studies of Solar Heating by CO2 in the Upper Atmosphere Using a Non-LTE Model and Satellite Data. J Atmospheric Sci 1990;47:809–22. https://doi.org/10.1175/1520-0469(1990)047<0809:SOSHBC>2.0.CO;2.

[56] López-Puertas M, Rodrigo R, López-Moreno JJ, Taylor FW. A non-LTE radiative transfer model for infrared bands in the middle atmosphere. II. CO2 (2.7 and 4.3 μm) and water vapour (6.3 μm) bands and N2(1) and O2(1) vibrational levels. J Atmospheric Terr Phys 1986;48:749–64. https://doi.org/10.1016/0021-9169(86)90023-1.

[57] López-Puertas M, Rodrigo R, Molina A, Taylor FW. A non-LTE radiative transfer model for infrared bands in the middle atmosphere. I. Theoretical basis and application to CO2 15

μm bands. J Atmospheric Terr Phys 1986;48:729–48. https://doi.org/10.1016/0021-9169(86)90022-X.

[58] Dang-Nhu M, Pine AS, Robiette AG. Spectral intensities in the v3 bands of 12CH4 and 13CH4. J Mol Spectrosc 1979;77:57–68. https://doi.org/10.1016/0022-2852(79)90196-6.

[59] McDowell RS. Rotational partition functions for spherical-top molecules. J Quant Spectrosc Radiat Transf 1987;38:337–46. https://doi.org/10.1016/0022-4073(87)90028-8.

[60] Gamache R, Vispoel B, Rey M, Tyuterev V, Barbe A, Nikitin A, et al. Non-Local Thermodynamic Equilibrium (NLTE) Total Internal Partition Sums (TIPS) for application to planetary atmospheres 2022. https://doi.org/10.5281/zenodo.6108004.

[61] Gordon IE, Rothman LS, Hill C, Kochanov RV, Tan Y, Bernath PF, et al. The HITRAN2016 molecular spectroscopic database. J Quant Spectrosc Radiat Transf 2017;203:3–69. https://doi.org/10.1016/j.jqsrt.2017.06.038.

[62] Laraia AL, Gamache RR, Lamouroux J, Gordon IE, Rothman LS. Total internal partition sums to support planetary remote sensing. Icarus 2011;215:391–400. https://doi.org/10.1016/j.icarus.2011.06.004.

[63] Bronnikov DK, Kalinin DV, Rusanov VD, Filimonov YUG, Selivanov YUG, Hilico JC. SPECTROSCOPY AND NON-EQUILIBRIUM DISTRIBUTION OF VIBRATIONALLY EXCITED METHANE IN A SUPERSONIC JET. J Quant Spectrosc Radiat Transf 1998;60:1053–68. https://doi.org/10.1016/S0022-4073(97)00210-0.

[64] Hilico JC, Baronov GS, Bronnikov DK, Gavrikov SA, Nikolaev II, Rusanov VD, et al. High-Resolution Spectroscopy of (Pentad-Dyad) and (Octad-Pentad) Hot Bands of Methane in a Supersonic Jet. J Mol Spectrosc 1993;161:435–44. https://doi.org/10.1006/jmsp.1993.1249.

[65] Gamache RR, Vispoel B, Rey M, Nikitin A, Tyuterev V, Egorov O, et al. Total internal partition sums for the HITRAN2020 database. J Quant Spectrosc Radiat Transf 2021;271:107713. https://doi.org/10.1016/j.jqsrt.2021.107713.

[66] Showman AP, Polvani LM. EQUATORIAL SUPERROTATION ON TIDALLY LOCKED EXOPLANETS. Astrophys J 2011;738:71. https://doi.org/10.1088/0004-637X/738/1/71.

[67] Brogi M, Kok RJ de, Albrecht S, Snellen IAG, Birkby JL, Schwarz H. ROTATION AND WINDS OF EXOPLANET HD 189733 b MEASURED WITH HIGH-DISPERSION TRANSMISSION SPECTROSCOPY. Astrophys J 2016;817:106. https://doi.org/10.3847/0004-637X/817/2/106.

[68] Seidel JV, Ehrenreich D, Pino L, Bourrier V, Lavie B, Allart R, et al. Wind of change: retrieving exoplanet atmospheric winds from high-resolution spectroscopy. Astron Astrophys 2020;633:A86. https://doi.org/10.1051/0004-6361/201936892.